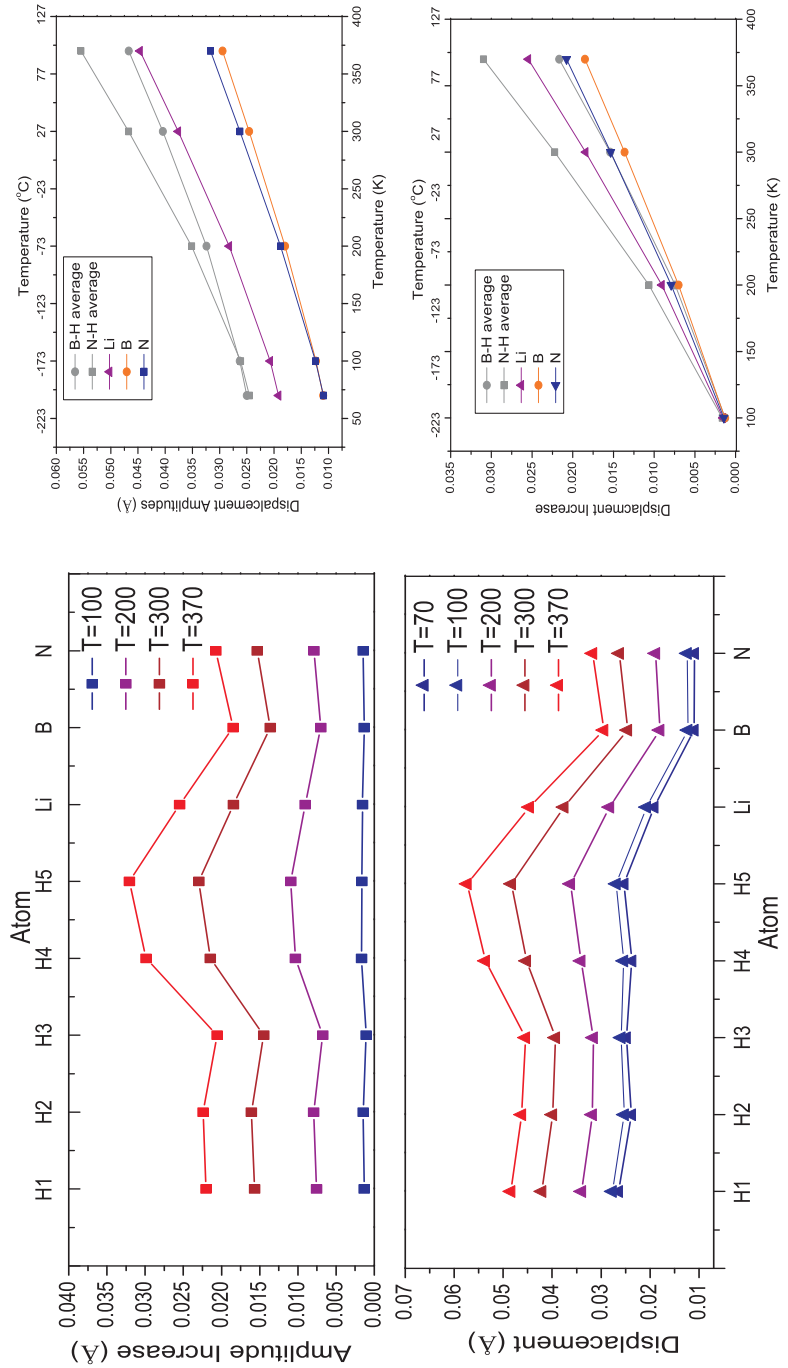

Figure 4.17: Graph showing how the atomic displacements of α-$LiNH_2BH_3$ change with temperature between 70K -370K (-203 to 97°C).

4.6 Variable Temperature INS of α-$LiNH_2{}^{11}BH_3$ on MAPS

Variable temperature INS measurements were made on the MAPS time-of-flight spectrometer at ISIS. A more complete experimental set up can be found in Section 2.3.4 but for clarity some of the essential details are repeated here. Spectra were collected at temperature points 13, 50, 100, 150, 300, 343, 367, 402K (-260, -223, -173, -123, 27, 70, 94, 129 °C) a range that went up to and beyond the decomposition point of α-$LiNH_2{}^{11}BH_3$. The combinations of (incident neutron energy E_i, Fermi chopper frequency, typical integrated beam current) used for the measurements were (200 meV, 400 Hz, 5,000 μA h), (300 meV, 450 Hz, 9,000 μA h) and (500 meV, 500 Hz, 7,000 μA h). A choice of lower E_i results in superior momentum and energy resolution, but can measure excitations only up to E_i so a range of E_i were used for each temperature. The raw data were mapped into S(Q,ω) and two-dimensional projections were produced by the MSlice software [148].

DFT calculations were performed using the CASTEP code to model the MAPS data. A comparison of the 13K 600 meV E_i experimental surface plot and theoretical surface plot generated from the DFT calculations are presented in Figure 4.18. There is very good overall agreement, despite the experimental data having a lower resolution, the areas of high intensity match very well. To allow the data to be visualised in a more traditional manner and a more in-depth peak analysis to be performed 'slices' of the surface plots were taken using the data were using the MSlice software [148]. The result was a series of standard INS spectra with Neutron energy loss in cm^{-1} along the x axis and S(Q,ω) along the y axis.

Figure 4.19(a) shows the VT spectral series at 13, 100, 300, 343, and 420K (-260, -173, 27, 70 and 147°C). Figure 4.19(b) shows spectra collected at 13K and 420K (-260°and 147°) along with the calculated spectra. The resolution is poor below 500 cm^{-1} as this region is outside the optimum energy window for the MAPS spectrometer. As with the surface plots, Above 500 cm^{-1} there is very good agreement between the calculated and the 13K (-260°C) spectra. The experimental peak shapes match the theoretical mode positions and intensities very well. Even more interestingly a number of the modes decrease and even disappear completely as the sample is heated through to decomposition, summarised in Table 4.4.

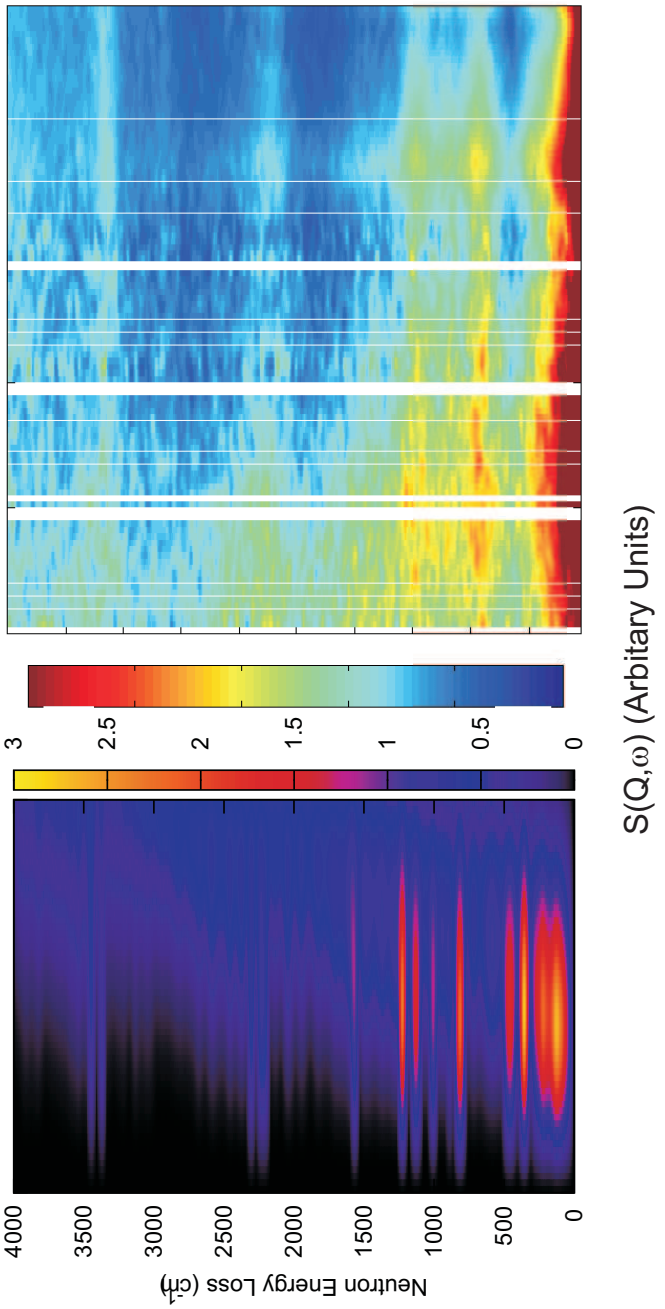

Figure 4.18: A comparison of the 13K 600 meV E_i experimental and theoretical surface plots of α-$LiNH_2{}^{11}BH_3$.

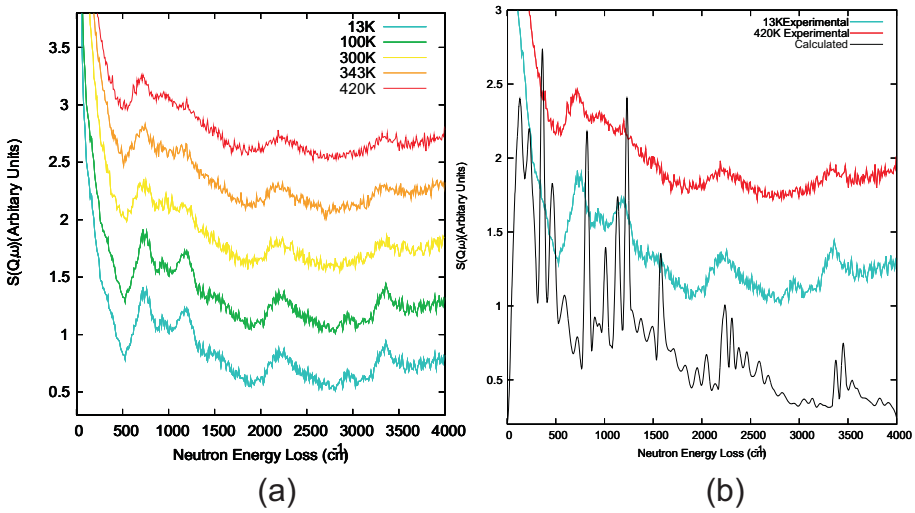

Figure 4.19: Graphs showing (a) the full VT range of the MAPs spectra collected at 600 E_i, (b) experimental spectra collected at 13K and 420K (-260°C and 147°C) at 600E $_i$ and the calculated spectrum. Spectra are offset and colour coded by temperature from blue to red for clarity.

The vanishing modes are hydrogenic, consistent with hydrogen being lost from α-$LiNH_2{}^{11}BH_3$ as it decomposes and the resulting lower H content of the residue. The co-operative N-H and B-H modes in the 1136 cm^{-1} - 1578 cm^{-1} region almost completely disappear. The symmetric N-H and B-H stretching modes are also greatly reduced which is to be expected as there are now fewer H bonds to vibrate. The N-H stretching mode decrease more sharply than the B-H modes which could be because there are fewer N-H bonds to start with.

The Li-N stretching modes (593 cm^{-1}) are faint due to the relatively low scattering cross-sections of Li and N but importantly they remain throughout the experiment and become more visible as some of the other mode decrease. This provides further evidence for a lithiated decomposition product.

Calculated Modes cm^{-1}	Mode Assignment	Modes disappearing at 420K
133	Anharmonic Lattice Vibration	
228	BH_3 Wagging	
359	BH_3 Libration	
467	NH_2 Libration	
593	N-Li Stretch	
720	N-Li Stretch + NH_2 Libration	
818	B-N Twisting	
907	B-N Stretch	
1014	B-N Rocking	
1136	BH_3 Umbrella mode	✓
1232	BH_3 Clapping mode	✓
1378	BH_3 Clapping mode	✓
1500	NH_2 Clapping mode	✓
1578	NH_2 Clapping mode	✓
1946	B-H Stretch symmetric	✓
2048	B-H Stretch symmetric	✓
2240	B-H Stretch (single)	
2313	B-H Stretch (double anti symm)	
2387	B-H Stretch (double anti symm)	
2467	B-H Stretch (double anti symm)	
2584	B-H Stretch (double anti symm)	
2684	B-H Stretch (double anti symm)	
3054	N-H Stretch symmetric	✓
3147	N-H Stretch symmetric	✓
3373	N-H Stretch symmetric	✓
3451	N-H Stretch antisymmetric	

Table 4.4: Wavenumbers and assignments for the observed modes of α-$LiNH_2BH_3$ in the MAPS spectra and how they change with temperature.

4.7 Decomposition Mechanism of α-$LiNH_2BH_3$

Combining of the crystallographic, thermogravimetric and spectroscopic data described in Sections 4.3, 4.4 and 4.5 has lead to a new decomposition mechanism being postulated. Many of the mechanisms suggested previously [185, 186, 187] have used gas phase or dimer calculations as the starting point, an approach that is computationally efficient but is not entirely realistic as the sample decomposes from the solid state. In the gas phase calculations the $LiNH_2BH_3$ molecules are free to re-orientate themselves to their most stable conformations but in reality the α-$LiNH_2BH_3$ crystal structure obviously restricts the conformations available as the molecules go through their initial decomposition step. The mechanism detailed below uses the thermal motion of the atoms within the crystal structure as the basis for the initiation step.

There are three stages to the mechanism illustrated in Figure 4.20

1. The strongly directional Li motion means it can move closer to its adjacent B atom and begins to abstract the closest $H^{\delta-}$ from it.
2. Once bound to the Li the $H^{\delta-}$ is close enough to interact with an $H^{\delta+}$ on the N atom. A bond forms between the two and H_2 is released leaving a N^- and B^+.
3. A bond then forms between the N^- and B^+ creating the lithiated polymer intermediate $(LiNHBH_2)_n$ suggested in Section 4.4.

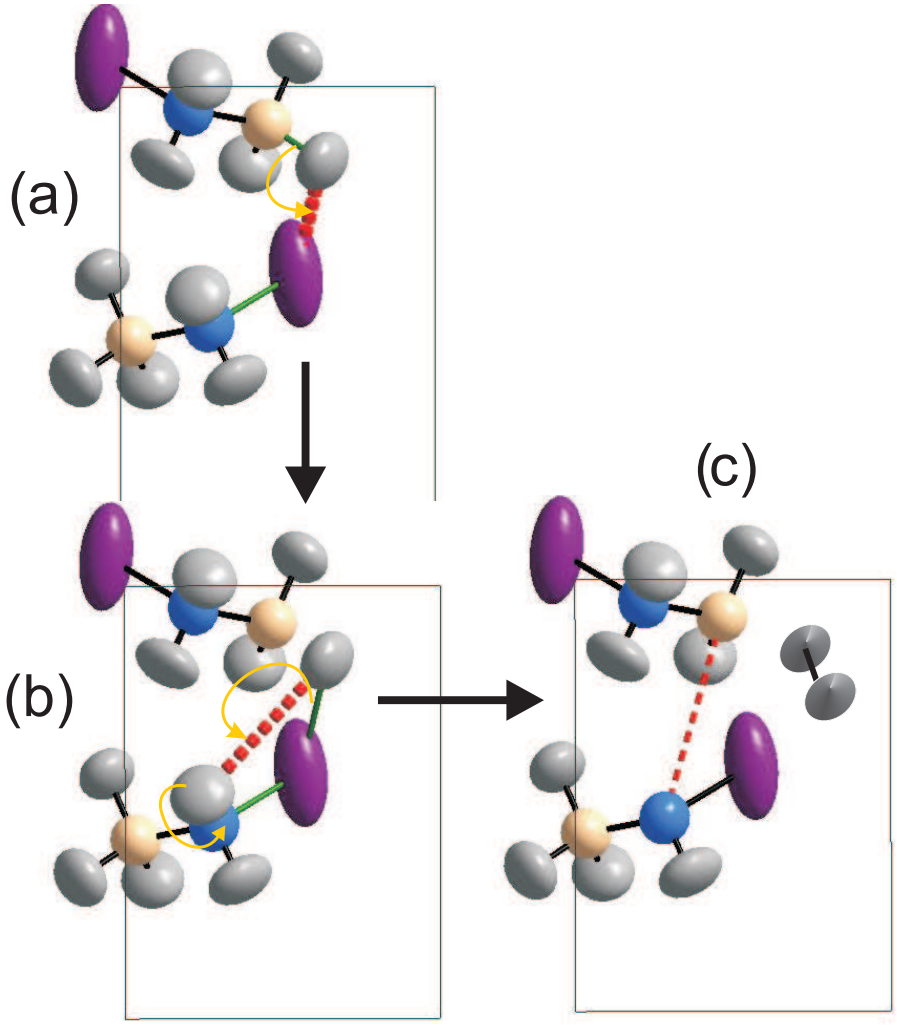

Figure 4.20: Schematic showing the possible decomposition mechanism of α-$LiNH_2BH_3$ using the crystal structure as the starting point.

4.8 Lithiated Tetragonal Phase

A new phase of $LiNH_2BH_3$ was found as trace impurity in various batches of $LiNH_2BH_3$ The phase was subsequently isolated and synthesised in high purity as described in Section 2.5.2. Despite an in-depth study utilising many characterisation techniques, the conflicting results they provided meant no definitive solution as to the structure, and indeed the stoichiometry, of this phase. Nevertheless, due to the significant proportion of research time devoted to the study of the lithiated tetragonal phase it was decided to present the data in this thesis. The results are presented below for the interested of the reader but no firm conclusions have been drawn.

4.8.1 NMR of the Lithiated Tetragonal Phase

NMR spectrum of the lithiated tetragonal phase was run by the Solid State NMR Research Service at the University of Durham. It was obtained using a Varian VNMRS spectrometer operating at 128.30 MHz for 11B and 399.88 MHz for 1H. The sample was packed into a (4 mm) rotor and run under nitrogen.

The NMR spectrum presented in Figure 4.21 is from a direct-polarisation^{11}B experiment with ^{1}H decoupling and a number of signals can be seen. Those below -50 and above +40 ppm are spinning sidebands. The intense line at -24 ppm is from a four-coordinate site, from [196] this would appear to be a BH_3N type environment. The quadrupolar bandshape between 0 and +30 ppm is typical of a B_2O_3 environment [197] suggesting some oxidation occurred during measurement. A simulation of the bandshape gave the quadrupole coupling constant as 2.75 MHz with asymmetry 0.2 and isotropic shift 30.5 ppm. Comparing intensities of lines from quadrupolar nuclei was not necessarily straightforward but for these two intense centre bands the integrated intensities are in the ratio 1:3.4. The other minor signals could be BH_2N_2 (8 ppm) BH_4 (-41 ppm) impurities [196].

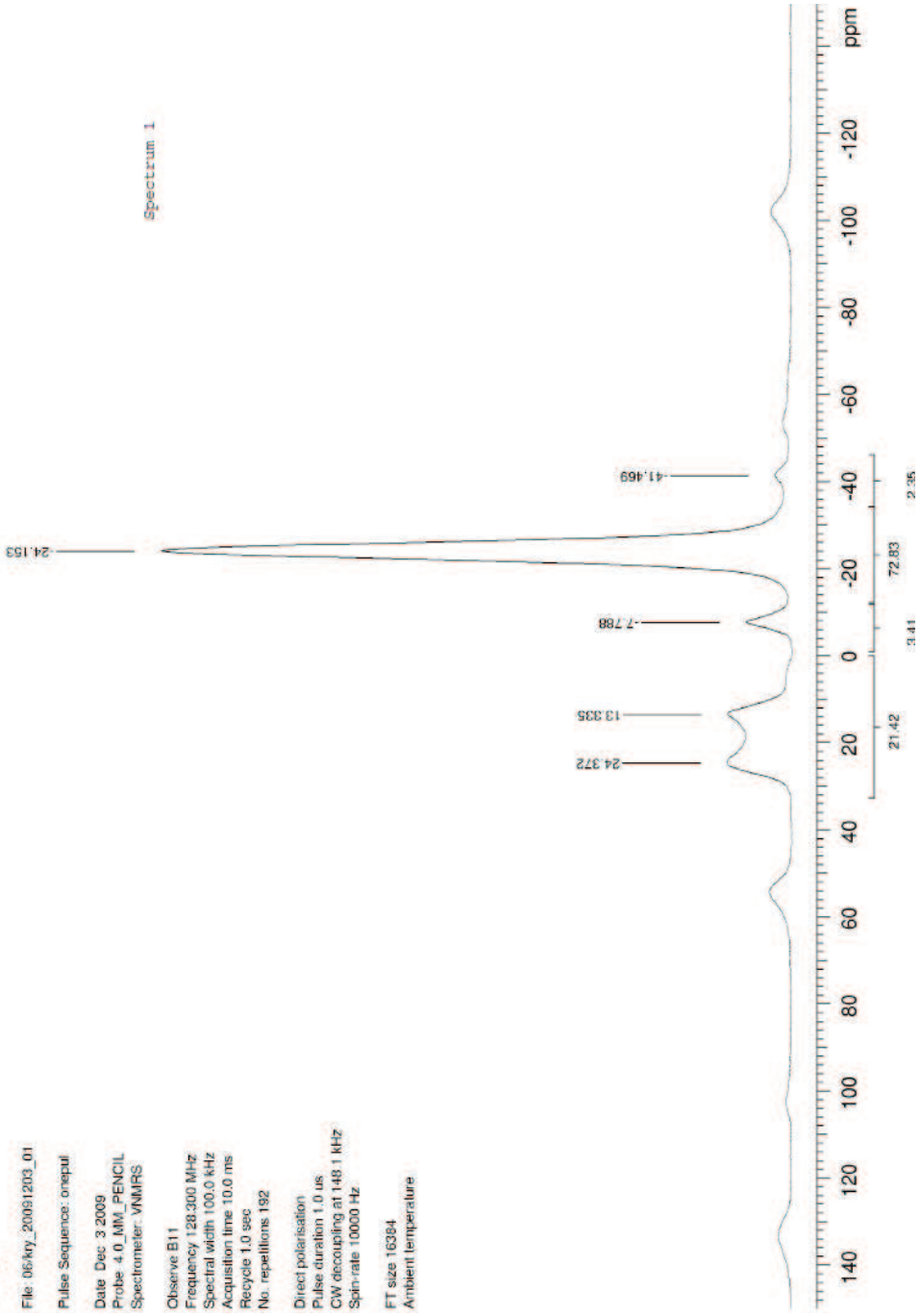

Figure 4.21: ^{11}B MAS NMR spetrum of the lithiated tetragonal phase.

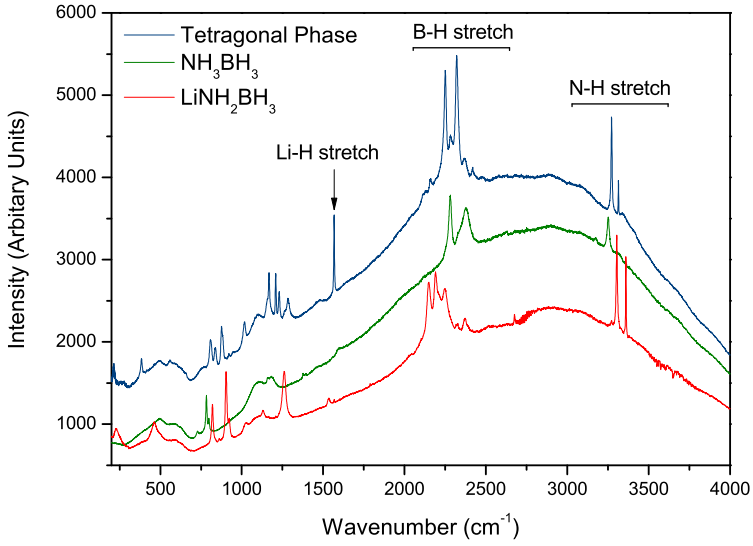

Figure 4.22: Experimental Raman spectra of the lithiated tetragonal phase (blue), NH_3BH_3 (green) and $\alpha LiNH_2BH_3$ (red) in the 0-2000 cm^{-1} region

4.9 Raman Study of Lithiated Tetragonal Phase

The Raman spectrum of the lithiated tetragonal phase is presented in Figure 4.22 along with the spectra of NH_3BH_3 and $\alpha LiNH_2BH_3$ to aid comparison (see Section 2.3.4 for experimental details). The most distinguishing feature of lithiated tetragonal phase spectrum is the very sharp peak at 1567 cm^{-1}. The origin of the the peak is an Li-H stretch [198] and indicates the presence of LiH or a lithium hydride like complex in the sample.

No crystalline LiH was detected in the X-ray diffraction pattern (see Figure 4.28) which infers that there may be an LiH containing amorphous compound in addition to the crystalline compound formed.

The B-H stretching region of lithiated tetragonal phase is more complex than those of NH_3BH_3 and $\alpha LiNH_2BH_3$, which is consistent with the presence of more than one B-H environment in the sample indicated by the NMR in Section 4.8.1.

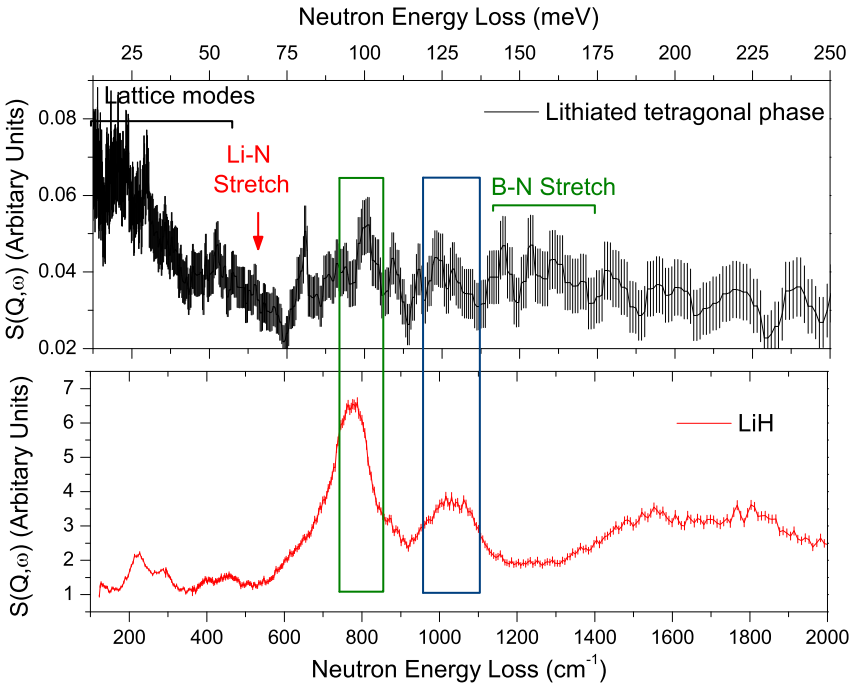

Figure 4.23: Experimental INS spectra of Tetragonal Phase $LiNH_2BH_3$ and LiH [199] in the 0-2000 cm^{-1} region.

4.10 Inelastic Neutron Scattering Studies of the Lithiated Tetragonal Phase

The INS data for the lithiated tetragonal phase were collected on the TOSCA INS spectrometer at ISIS (Section 2.3.4) before the structure was known. This meant there was nothing to compute the phonon density of states from and the modes could not be exactly assigned. Furthermore the observed peaks are rather ill defined possibly due to the greater degree of disorder in the tetragonal structure reducing the coherent scattering. However using data from the α-$LiNH_2BH_3$ phonon density of states it has been possible to assign regions of the spectrum, presented in Figure 4.23.

In an attempt to corroborate the Li-H stretch found in the Raman spectrum the lithiated tetragonal INS spectrum is also presented with the LiH INS spectrum. It can be seen that there are similarities between the two, namely the two broad peaks at 800 and 1030 cm^{-1}.

4.11 In-Situ synthesis of the Tetragonal Phase in the IGA

The tetragonal phase can be made easily via the solid state reaction of LiH + $2NH_3BH_3$ (Section 2.5.2). One very interesting feature of this synthesis method is that the sample foamed and almost quadrupled in volume. This indicated two things

1. A large amount of gas was evolved during the reaction
2. The gas was probably evolved from a more mobile /liquid intermediate state

It was hoped that by determining which gas/gases and how much of them were evolved during the synthesis would provide more information on the nature of the product and resolve the differences observed in the crystallographic and spectroscopic data. As such it was decided to try and replicate the synthesis conditions in the IGA so the reaction could be monitored *in-situ*.

LiH (5mg) and $2NH_3BH_3$ (38mg) were ground and loaded, under inert conditions, into the IGA-MS apparatus as outlined in Section 2.3.1. In a change to the usual experimental procedure a larger quartz bucket was used instead of the regular mesh one. This was to accommodate any foaming and prevent any liquid intermediates escaping. In accordance with the known synthesis conditions, the sample was heated at 2°C min^{-1} under 1 bar of flowing He (100ml min^{-1}) to 353K (80°C), and held there for 12 hours. A small aliquot of the outgoing gases were diverted to the dynamic sampling mass spectrometer, which was set to scan for materials of 2, 14, 17, 28 and 81 atomic mass units (AMU), corresponding to, H_2, NH_3, B_2H_6, $B_3N_3H_6$, respectively. Measurements of the sample mass (mg), temperature (°C), pressure (mbar), and the partial pressures of the released gases (μTorr) were taken every 0.2 minutes.

The results from the IGA experiment are shown in Figure 4.24. A mass loss of 19.3% was observed in the early stages of the isothermal region of the experiment. The mass loss appeared to be a single event. However, differentiation of the mass loss with respect to time (see Figure 4.25 inset) revealed two, almost overlapping, events with maxima at 62 and 67 minutes.

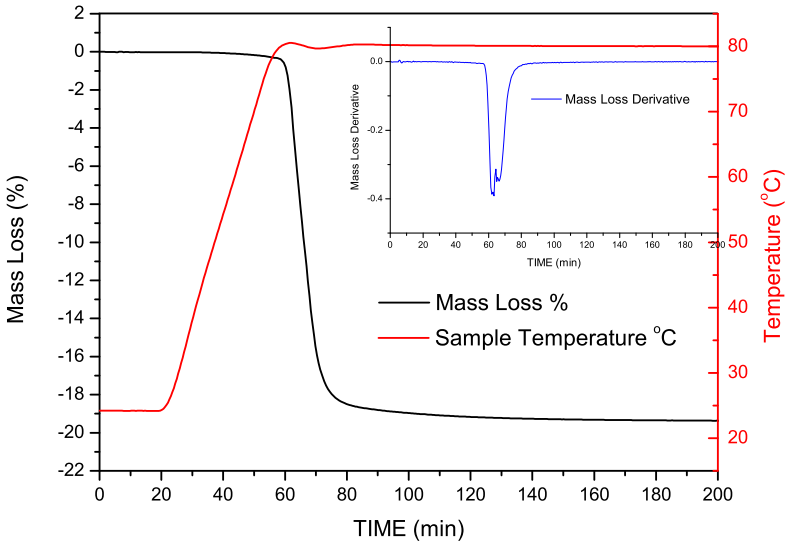

Figure 4.24: Thermogravimetric data of the insitu formation of tetragonal phase of lithium amidoborane collected using intelligent gravimetric analysis, with heating rate 2°C min^{-1} and target temperature of 80°C (353K). The red line represents the temperature of the sample and the black line the sample mass loss in %. Insert: differential of sample mass loss % with respect to temperature

The mass spectrometry data, showing the partial pressures of NH_3 (17 AMU) and H_2 (2 AMU) evolved from the sample as a function of time, are presented in Figure 4.25, with the thermogravimetric data added to aid comparison. It is clear from this data that the observed mass loss was primarily due to the production of H_2, with a small proportion of NH_3 also formed (note the difference in scale on the graph axes). The peak evolution of these gases agrees well with the peaks observed in the mass loss differentiation, with the H_2 maximum at 62 min and the NH_3 maxima at 67 min.

The 19.3 mass loss % from the sample is considerably lower than the theoretical mass loss of 28.0%, expected for a product consistent with the elemental analysis results (H 15.83%, C <0.01%, N 27.72%). However, the sample sent for elemental analysis had to be placed under vacuum when it was removed from the furnace to allow it to be taken into the glove box, whereas the sample formed *in-situ* was not. Therefore, due to the adhesive nature of NH_3 it is highly plausible that some of the NH_3 formed remained

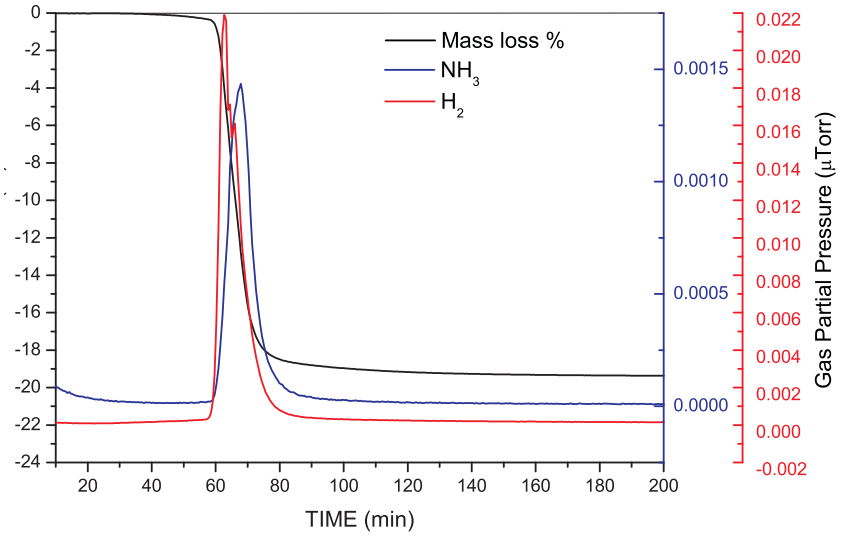

Figure 4.25: Thermogravimetric data of the 'in-situ' formation of tetragonal phase of lithium amidoborane collected using intelligent gravimetric analysis, with heating rate 2°C min^{-1} and target temperature of 80°C (353K). The partial pressures of NH_3 (blue line) and H_2 (red line), recorded using in-situ mass spectrometry are also presented.

adsorbed to the sample (only to be released later when the sample was decomposed see Section 4.12). Additionally elemental analysis has been found to be unreliable for some more complex B-N compounds due to the complex nature of the decomposition products [200]. A general reaction is outlined below:

$$2LiH + 4NH_3BH_3 \rightarrow xNH_3 \uparrow + yH_2 \uparrow + Li_2N_{(4-x)}B_4H_{(26-(3x+2y))}$$

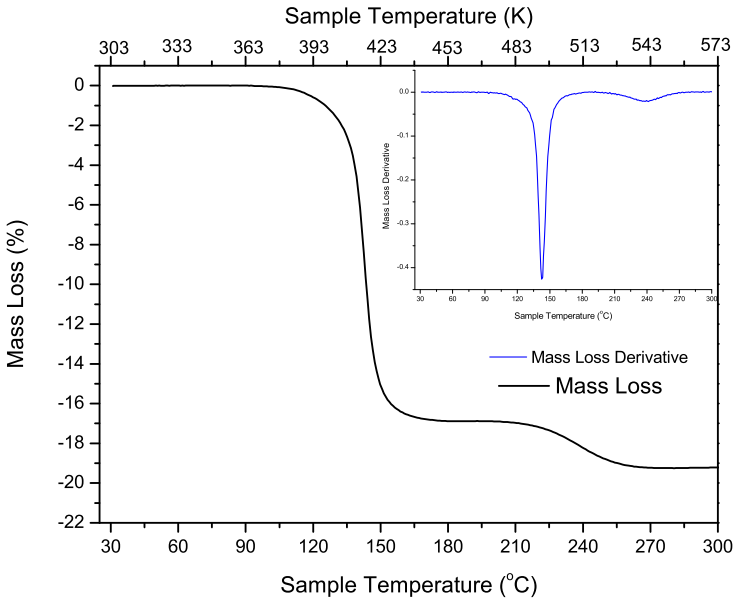

Figure 4.26: Thermogravimetric data of the decomposition of tetragonal phase of lithium amidoborane collected using intelligent gravimetric analysis, with heating rate 2°C min^{-1} and target temperature of 300°C (573K). The black line represents the sample mass loss in %. Insert: differential of sample mass loss % with respect to temperature

4.12 Intelligent Gravimetric Analysis of the Decomposition of the Lithiated Tetragonal Phase

The thermogravimetric data for the decomposition of tetragonal phase of lithium amidoborane, measured using the IGA-MS apparatus (Section 2.3.1, are presented in Figure 4.26. A total mass loss of 19.2% was observed over two events. The first mass loss event of 16.8% commenced at 102°C (375K) and the second mass loss event of 2.3% started 100 degrees later at 203°C (476K). Differentiation of the mass loss with respect to temperature (see Figure 4.26 inset) confirmed these findings and revealed peak mass losses of the two events to be at 143°C and 238°C (416K and 511K).

The mass spectrometry data, showing the partial pressures of NH_3 (17 AMU) and H_2 (2 AMU) evolved from the sample as a function of temperature, are presented in Figure 4.27, with the thermogravimetric data added to aid comparison. It is clear from this data that the observed mass loss was primarily due to the production of H_2, with a small proportion of NH_3 also formed (note the difference in scale on the graph axes). The peak evolution of these gases agrees well with the peaks observed in the mass loss differentiation. H_2 is released in both mass loss events with maxima found at 144°C and 239°C (417 and 512K). Integration of the area under the peaks gave an approximate ratio of 1.25 : 1.

The partial pressure of NH_3 evolved is 60 times less than the hydrogen partial pressure and the data are more difficult to deconvolute. There is a clear peak at 143°C (416K) accompanying the first mass loss event but not for the second and the signal becomes smeared out. This lag could be due to some residual NH_3 becoming adsorbed to the sample and instrument walls.

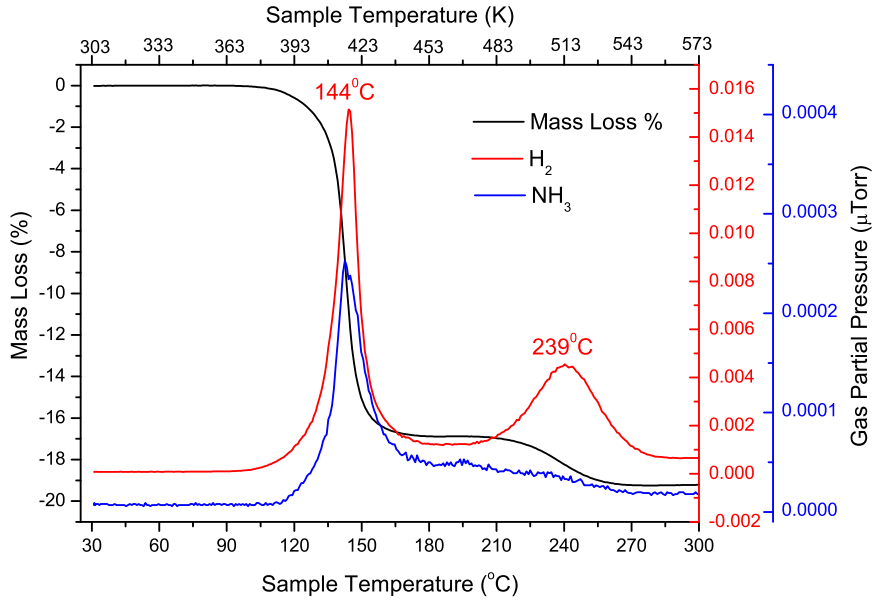

Figure 4.27: Thermogravimetric data of the decomposition of the tetragonal phase of lithium amidoborane collected using intelligent gravimetric analysis, with heating rate 2°C min^{-1} and target temperature of 300°C (573K). The partial pressures of NH_3 (blue line) and H_2 (red line), recorded using in-situ mass spectrometry are also presented.

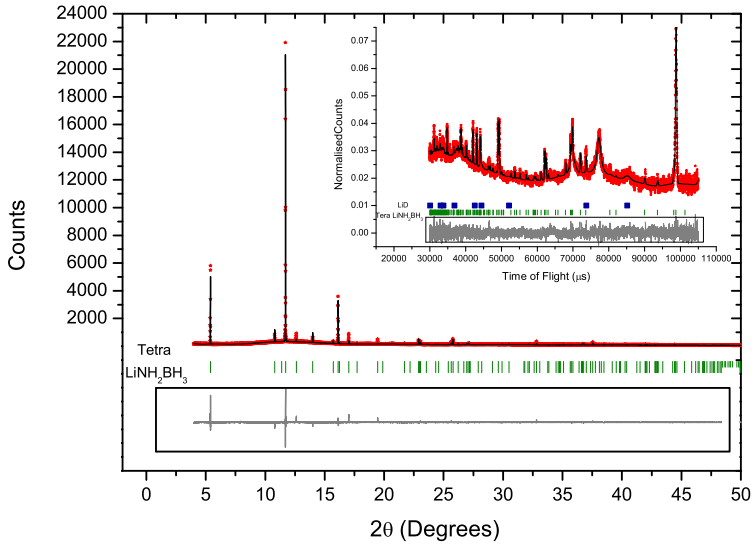

Figure 4.28: Final Rietveld refinement plots for X-ray and neutron (inset) diffraction data showing observed (blue) , calculated (red) and difference (grey) plots. Bragg peak positions for the lithiated tetragonal phase (green) are indicated.

4.13 Crystal Structure of the Lithiated Tetragonal Phase

The structure was solved using the combination of data collected at the ESRF in Grenoble and on GEM at ISIS (Section 2.2.3).

The X-ray diffraction data were indexed in TOPAS [125] to a tetragonal unit cell $a = b = 4.0288(3)$Å $c = 16.984(4)$Å but there was some uncertainty as to the space group.

Initial attempts to solve the structure used charge flipping, a recently developed algorithm of *ab initio* structure determination [201]. Charge flipping is based on the perturbation of large plateaus of low electron density but not directly on atomicity and and offers complementary applications to the classical methods described in Section 2.2.4. The simulations did not give any conclusive results, suggesting a large amount of disorder within the unit cell. However, there was one consistent feature - five atom chains.

As the NMR data presented in section indicated a BH_3 environment and the IGA data from the formation showed the release of NH_3 it was concluded that the most probable composition of the 5 atom string was BH_3-NH_2-BH_2-NH_2-BH_3.

Still using the X-ray data, a skeleton B-N-B-N-B z-matrix was constructed in TOPAS (to simplify things initially the H atoms were left of initially for the sake of simplicity as their overall contribution to the X-ray data was deemed to be negligible). This skeleton along with a Li atom was used for simulated annealing in the *P-4* space group. However, this generated too many reflections.

Pawley refinements with a range of other tetragonal space groups were performed in an attempt to find a better fit with a higher symmetry group. The best fit was found to be for *P-42c*. The simulated annealing experiment was run again the and the Z-matrix reduced to a $BH_3NH_2BH_2$ unit to allow for the <004> mirror plane.

The best result from the simulated annealing was used as the starting point for Rietveld refinement with the atomic positions still restrained using Z-matrices.

Once a good fit had been achieved a new Rietveld refinement was set up using the neutron data so that the D positions could be found. D atoms were added to the z-matrix and allowed to refine and rotate.

Finally a simultaneous refinement of the neutron and X-ray data sets was performed to resolve the two structures. A fit of χ^2 =2.51 was achieved and the final atomic coordinates are given in Table 4.5 and the structure shown in Figure 4.29.

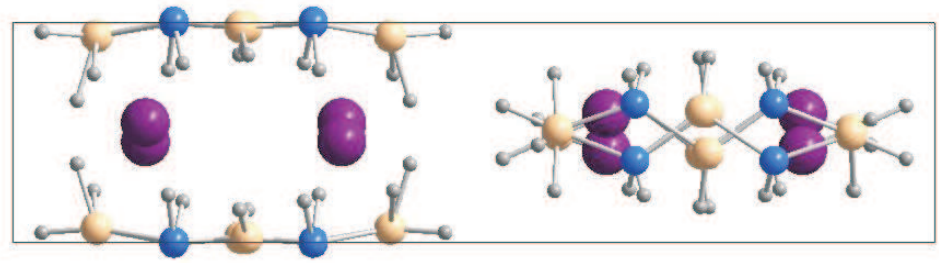

Figure 4.29: Structural diagram of lithiated tetragonal phase viewing along the *b* axis. Lithium is purple, nitrogen blue, and boron cream.

Atom	x/a	y/b	z/c	Occupancy	B_{iso} Å^2	Wyckoff Positions
B1	0.0630	0.4902	0.9093	1.00	6.3	8c
B2	-0.0217	0.5956	0.7533	0.50	6.3	8c
N1	-0.0038	0.3710	0.8255	0.50	0.1	8c
Li1	0.4568	0.4167	0.8565	0.50	3.4	8c
H6	0.1862	0.2143	0.8159	0.50	4.5	8c
H4	0.3561	0.44198	0.9306	0.33	4.5	8c
H7	0.1483	0.8386	0.7546	0.50	4.5	8c
H8	-0.2162	0.2425	0.8317	0.50	4.5	8c
H9	0.2349	0.2342	0.9125	1.00	4.5	8c
H10	-0.0442	0.6203	0.9688	1.00	4.5	8c

Table 4.5: Refined crystallographic data for the lithated tetragonal phase space group *P-42c* a=4.0288(3)Å, c=16.984(4) Å R_{wp} = 8.120 R_{exp} = 5.436 χ^2 = 2.51.

4.14 Conclusions

Two phases of $LiNH_2BH_3$ (α and β) and a lithiated subsidiary phase have been identified and their structures solved.

α-$LiNH_2BH_3$ was synthesised in a one-pot room temperature reaction between LiH and NH_3BH_3 in diethyl ether. The structure of α-$LiNH_2BH_3$ was investigated by neutron powder diffraction and synchrotron X-ray powder diffraction. The neutron and X-ray data were refined simultaneously and α-$LiNH_2BH_3$ was identified to have the space group *Pbca* with a single Li site and room temperature lattice constants of a = 13.94682(7)Å, b = 5.14883(3)Å, c = 7.11254(3)Å.

β-$LiNH_2BH_3$ was synthesised via high energy milling between LiH and NH_3BH_3. The structure of α-$LiNH_2BH_3$ was investigated by synchrotron X-ray powder diffraction. The X-ray data were refined and β-$LiNH_2BH_3$ was identified to have the space group *Pbca* with two lattice sites and room temperature lattice constants of a =15.146(6)Å, b = 7.721(3)Å, c = 9.268(4)Å.

A variable temperature synchrotron X-ray diffraction study of α-$LiNH_2BH_3$ was also completed. The lattice parameters of α-$LiNH_2BH_3$ increased linearly with increasing temperature from 200K-360K (-73°C to 87°C) where upon they began to deviate from the fit with a complete loss of crystallinity at 367K (94).

A thermogravimetric analysis with mass spectrometry study of α-$LiNH_2BH_3$ was performed. α-$LiNH_2BH_3$ was heated to to 250 °C (673K) under 1 bar of flowing He (100ml min^{-1}). The sample lost 5.8% of its weight over two decomposition events. The events had maxima at 92°C (365K)and 110°C(383K) respectvly. The mass spectrometer detected hydrogen as the major decomosition product along with trace amounts of ammonia.

A DSC trace of α-$LiNH_2BH_3$ was collected and showed two exotherms with maxima at at 91°C (364K), and 131°C (404K) respectively.

The full phonon density of states was calculated by DFT which allowed comparison the INS spectra (collected on TOSCA and MAPS) and the Raman spectrum. The calculations were also used to model the atomic motion up to the decomposition temperature of α-$LiNH_2BH_3$.

Combination of the crystallographic, thermogravimetric and vibrational information allowed a decomposition mechanism to be proposed for the decomposition of α-$LiNH_2BH_3$.

The lithiated tetragonal phase was synthesised from the solid state reaction of 2LiH + $4NH_3BH_3$. The reaction was followed *in situ* by thermogravimetric analysis and believed to form via the following reaction along with an amorphous adduct:

$$2LiH + 4NH_3BH_3 \rightarrow x NH_3 \uparrow + y H_2 \uparrow + Li_2N_{(4-x)}B_4H_{(26-(3x+2y))}$$

The lithiated tetragonal phase was investigated by neutron powder diffraction and synchrotron X-ray powder diffraction. The neutron and X-ray data were refined simultaneously and the lithiated tetragonal phase was identified to have the space group *P-42c* with room temperature lattice constants of $a = 4.0288(3)$ Å, $c = 16.984(4)$ Å.

The decomposition of the lithiated tetragonal phase was also studied by thermogravimetric analysis with mass spectrometry. The sample lost 19.2% of its weight over two decomposition events. The events had maxima at 144°C (417K) and 239°C (512K) respectively. The first step evolved hydrogen and ammonia (believed to be residual from the formation reaction) and the second mainly hydrogen.

The INS and spectra of the lithiated tetragonal phase were collected. Complete assignment of the modes was not possible due to the lack of a crystal / molecular structure at the time of doing the calculations but general regions of the spectra could be identified.

Chapter 5

Sodium Amidoborane

5.1 Introduction and Chapter Outline

The formation of $NaNH_2BH_3$ in solution was reported in 1938 [202]. Schlesinger identified a substituted ammonia borane species from the reaction of $(CH_3)_2OBH_3$ and Na in liquid ammonia. However, no crystallographic or decomposition information on $NaNH_2BH_3$ was reported until 2008 when Xiong *et al.* published their paper on metal amidoboranes as hydrogen storage materials [86].

Xiong *et al.* found $NaNH_2BH_3$ to be isostructural with α-$LiNH_2BH_3$ crystallizing in the orthorhombic space group *Pbca* with lattice parameters of a =7 .46931(7) Å, b = 14.65483(16) Å, c = 5.65280(8) Å, V = 618.764(20) Å^3. They did not publish the atomic coordinates but their findings were confirmed by *ab initio* calculations by Ramzan *et al* [176]. Additionally, because $NaNH_2BH_3$ is isostructural with α-$LiNH_2BH_3$, the experimental structure of α-$LiNH_2BH_3$ published by Wu *et al.* [91] is also of use.

Initially crystalline samples of $NaNH_2BH_3$ were formed using high impact ball milling synthesis techniques [86]:

NH_3BH_3 (s) + NaH (s) $\rightarrow$ $NaNH_2BH_3$ (s) + H_2(g)$\uparrow$

This technique suffers from a number of disadvantages, that have been discussed previously in Section 4.1 and therefor solution-based routes were developed using NaH or $NaNH_2$ and NH_3BH_3 in THF [97] [203] [180].

Despite the initially positive findings that approximately 7.5 wt% hydrogen is evolved below 100°C (373K) with no borazine production [86] there is very little published about $NaNH_2BH_3$ in the litereature. This could be due in part, to the 2009 article by Fijakowski *et al.* [96] who found substantial emission of NH_3 during thermal decomposition of $NaNH_2BH_3$.

NMR findings for $NaNH_2BH_3$ are similar to those for $LiNH_2BH_3$ with a solid state MAS $^{11}BH_3$ shift of *ca.* -20ppm [86] [96]. This is deshielded with respect to the $^{11}BH_3$ shift of NH_3BH_3 suggesting electron withdrawal by the Na metal from the BH_3 units in the crystal structure.

Two decomposition mechanisms have been proposed for $NaNH_2BH_3$. Both are based on a 'head-to-tail' dimerization pathway but that is where the similarity ends. To explain their observed NH_3 emission, Fijakowski *et al.* [96] suggest the formation of the salt $[NH_3Na]^+[BH_3(NHNa)BH_3]^-$. The $[NH_3Na]^+[BH_3(NHNa)BH_3]^-$ can then decompose easily to release NH_3 and the remaining salt to release H_2:

$$[NH_3Na]^+[BH_3(NHNa)BH_3]^- \rightarrow [Na]^+[BH_3(NHNa)BH_3]^- + NH_3\uparrow$$

$$[Na]^+[BH_3(NHNa)BH_3]^- \rightarrow NaH + BH_3(NHNa)BH_2$$

$$BH_3(NHNa)BH_2 \rightarrow BH_2(NNa)BH_2 + H_2\uparrow$$

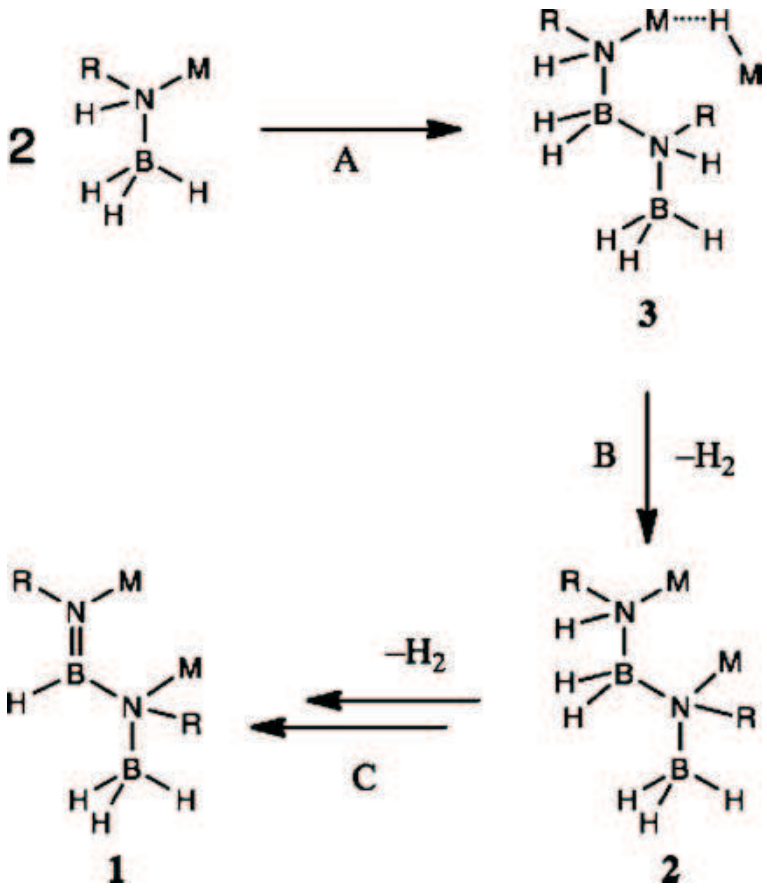

Figure 5.1: Generalised metal amidoborane decomposition mechanism [180]

In contrast, Luedtke and Autrey [180] suggested the formation of polymeric B-N-H species that evolves pure hydrogen as a part of a generalised metal amidoborane decomposition mechanism:

$2NaNH_2BH_3 \rightarrow$ Na-H$\cdots$Na-$NH_2BH_2NH_2BH_3$

Na-H$\cdots$Na-$NH_2BH_2NH_2BH_3 \rightarrow NaNHBH_2NaNHBH_3 + H_2\uparrow$

$NaNHBH_2NaNHBH_3 \rightarrow$ NaHN=BHNNaHBH $H_2\uparrow$

In this chapter, the structure of $NaNH_2BH_3$ is explored in detail with synchrotron X-ray powder diffraction at the SLS on the MS X04SA high-resolution beamline and neutron powder diffraction on GEM at ISIS (Section 5.2). Variable temperature synchrotron X-ray powder diffraction experiments were also undertaken to monitor the changes in crystal structure up to decomposition (Section 5.3). Hydrogen desorption properties were studied using combined intelligent gravimetric analysis with mass spectrometry (IGA-MS, Section 5.4) and potential decomposition mechanisms discussed.

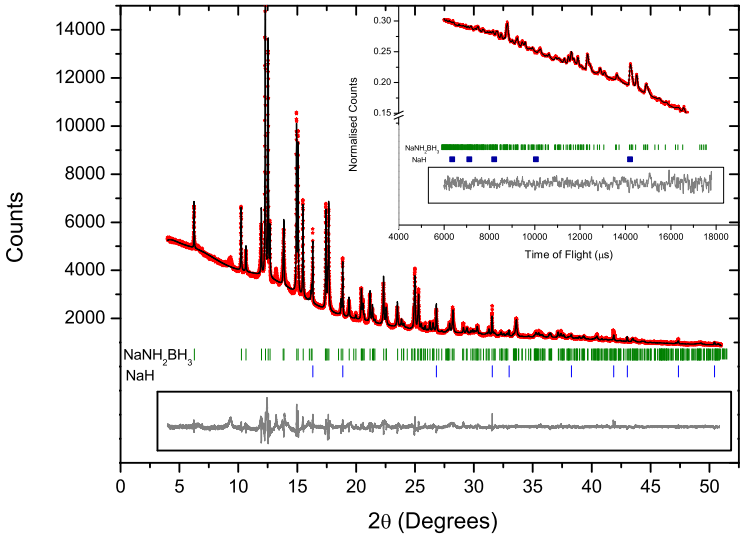

Figure 5.2: Final Rietveld refinement plots for X-ray and neutron (inset) diffraction data showing observed (red dots) , calculated (black line) and difference (grey) plots. Bragg peak positions for the $NaNH_2BH_3$ (green) and NaH (blue)are indicated.

5.2 Crystal Structure of $NaNH_2BH_3$

The final refinement presented in this thesis was obtained from a simultaneous Rietveld analysis of synchrotron X-ray data from the SLS on the MS X04SA high-resolution beamline (see Section 2.2.2)and neutron powder diffraction data (Figure 5.2) and consequently enable the H positions to be determined with a high degree of accuracy. Notably, the neutron data was collected on samples with naturally occurring isotopes on the GEM powder diffractometer at ISIS (Section 2.2.3). The presence of natural boron results in very high absorption which dramatically reduces the diffraction signal, while the incoherent scattering contribution from the hydrogens results in a large background (Figure 5.2 inset). Nevertheless, the high count rate of GEM can enable diffraction patterns of sufficient quality for accurate refinement to be collected in approximately four hours.

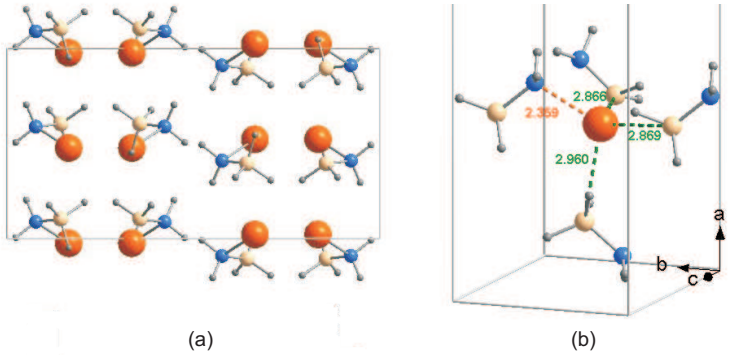

Figure 5.3: Structural diagram of $NaNH_2BH_3$ (a)viewing along the b axis, (b) tetrahedral electrostatic interactions between Na^+ and the 3 closest BH_3 units. (All bond lengths in Angstroms calculated from refined powder data.) Sodium is orange, nitrogen blue, and boron cream.

$NaNH_2BH_3$ was found to be isostructrual with α-$LiNH_2BH_3$ with Li^+ and Na^+ occupying the same atomic sites (Figure 5.3) but with expanded lattice constants a = 14.6474(32)Å b = 5.6548(09)Å c = 7.4680(16)Å. The atomic coordinates are shown in Table 5.1

There are two principal differences between the structures of α-$LiNH_2BH_3$ and $NaNH_2BH_3$, both of which arise from the larger ionic radius of sodium (Li^+ = 76 pm Na^+ = 102pm) [204] . The M-N bond length increases from 1.99(4) Å to 2.32(3) Å in an analogous trend to the corresponding amides ($LiNH_2$ 2.13 Å [188] to $NaNH_2$ 2.44 Å [205]). This separates the $NaNH_2BH_3$ molecules to a greater degree than α-$LiNH_2BH_3$ resulting in an expanded unit cell.

There is little change in the $[NH_2BH_3]^-$ unit on replacement of Li^+ with Na^+. The N-H bonds lengthen with respect to α-$LiNH_2BH_3$ (0.99(2) Å on α-$LiNH_2BH_3$, 1.03(1) Å on $NaNH_2BH_3$) probably due to the increased steric repulsion from the Na^+.

Atom	x/a	y/b	z/c	Occupancy	B_{iso} / Å^2	Wyckoff Positions
B	0.1500300	0.036470	0.103510	1	2.4441	8c
H1	0.1073566	-0.13982	0.182589	1	3.1204	8c
H2	0.2216664	0.0982673	0.192206	1	3.1204	8c
H3	0.1811787	-0.035689	-0.048619	1	3.1204	8c
N	0.0899679	0.283161	0.068662	1	2.4179	8c
H4	0.0303835	0.245799	-0.002018	1	4.8876	8c
H5	0.0559582	0.351845	0.180261	1	4.8876	8c
Na	0.1795554	0.553818	-0.027695	1	3.7997	8c

Table 5.1: Atomic coordinates of $NaNH_2BH_3$ X-ray data - $R_{wp} = 1.66$ $R_{exp} = 0.72$ $\chi^2 = 2.31$ Neutron Data - $R_{wp} = 1.31$ $R_{exp} = 0.69$ $\chi^2 = 1.90$.

$NaNH_2BH_3$ was the most difficult phase to characterise in this thesis. It was even more susceptible to radiation damage than α-$LiNH_2BH_3$, to the extent where no refineable patterns could be collected at the ESRF as the high flux of the beam seemed to decompose it to NaH and an amorphous compound. $NaNH_2BH_3$ also degrades over a period of weeks, when stored under inert conditions, to an amorphous compound.

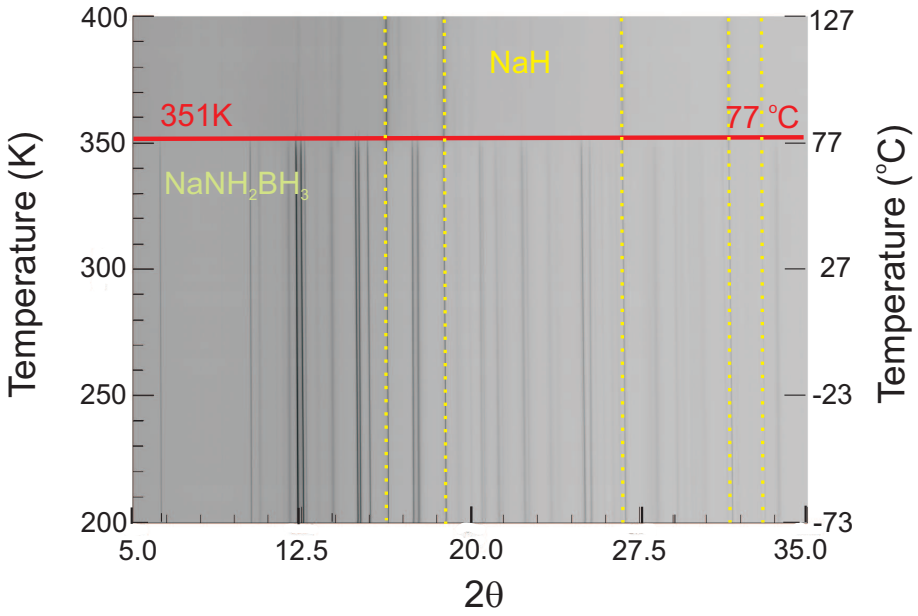

Figure 5.4: Surface plot of synchrotron X-ray diffraction data collected during the heating of $NaNH_2BH_3$ 400K in a sealed glass capillary tube. Lines corresponding to Bragg reflections of NaH are highlighted indexed.

5.3 Variable Temperature X-ray Diffraction Studies of $NaNH_2BH_3$

Variable temperature X-ray powder diffraction patterns of $NaNH_2BH_3$ were collected between 200-400K in 1K steps on MS X04SA, the high-resolution beamline at the SLS (see Section 2.2.2) The data sets were refined sequentially in a batch file as detailed in Section 2.2.4.

Inspection of the Bragg peaks during variable temperature X-ray diffraction experiments reveals peak broaden and flattening with increasing temperature, with a complete disappearance of crystalline $NaNH_2BH_3$ at 351K (78°C) (see Figure 5.4). Sequential refinement of the diffraction patterns revealed all the lattice parameters to increase linearly with temperature, but with significant anisotropic expansion The a axis expanded by +0.96% , the b axes by +0.29% and the c axis by +0.78% as shown in Figure 5.5a.

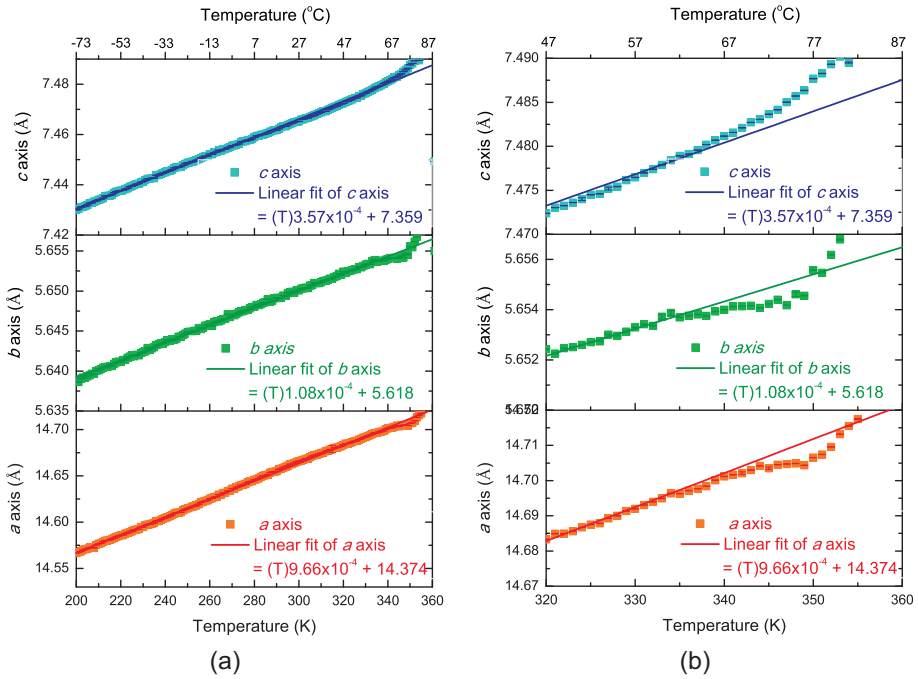

Figure 5.5: Refined $NaNH_2BH_3$ lattice parameters, calculated from Rietveld analysis of synchrotron diffraction data (via batch refinement) collected during the heating of $NaNH_2BH_3$ to 400K (127°C). Mean errors, $a \pm 0.00008$, $b \pm 0.00002$ $c \pm 0.00003$. Error bars only shown if larger than data markers.

Above 345K (72°C) the lattice parameters begin to deviate from their linear fits (Figure 5.5(b).) before a complete loss of crystallinity at 351K (78°C). The c axis lengthens and the a and b contract (briefly) before decomposition. Refinement of anisotropic displacement parameters (ADPs) for the Na, B and N using the data collected at 350K (77°C) provides a clear explanation for the anomalous lattice behaviour. As can be seen from Figure 5.6 the Na motion is large and very anisotropic. The dominant displacement is along the U_{22} ellipsoid parameter which corresponds to the lengthening c axis in the unit cell.

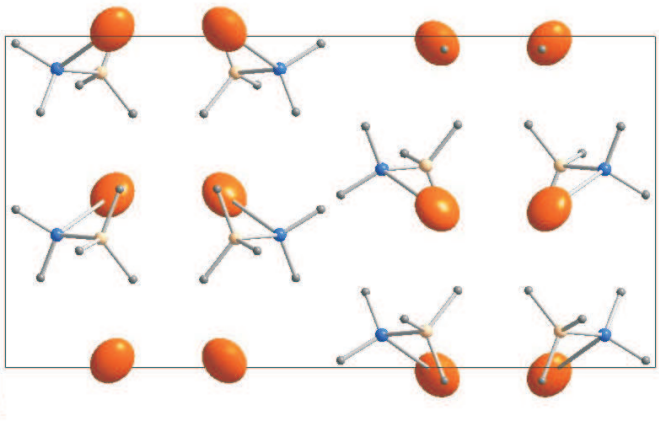

Figure 5.6: Structural diagram of $NaNH_2BH_3$ with refined ADPs for the Na atoms (ellipsoid probability 1) viewing along the b axis. Sodium is orange, nitrogen blue, and boron cream.